Supplementary Information for

Mid-latitude ozone depletion and air quality impacts from industrial halogen emissions in the Great Salt Lake Basin

Caroline C. Womack[1,2*], Wyndom S. Chace[3†], Siyuan Wang[1,2], Munkhbayar Baasandorj[4], Dorothy L. Fibiger[1,2‡], Alessandro Franchin[1,2#], Lexie Goldberger[5§], Colin Harkins[1,2], Duseong S. Jo[6], Ben H. Lee[5], John C. Lin[4], Brian C. McDonald[2], Erin E. McDuffie[1¶], Ann M. Middlebrook[2], Alexander Moravek[7||], Jennifer G. Murphy[7], J. Andrew Neuman[1,2], Joel A. Thornton[5], Patrick R. Veres[2], Steven S. Brown[2,8]

1) *Cooperative Institute for Research in Environmental Sciences, University of Colorado, Boulder, CO 80309*
2) *NOAA Chemical Sciences Laboratory, Boulder, CO 80305*
3) *Department of Chemistry, Williams College, Williamstown, MA 01267*
4) *Department of Atmospheric Sciences, University of Utah, UT 84112*
5) *Department of Atmospheric Science, University of Washington, Seattle, WA 98195*
6) *Atmospheric Chemistry Observations and Modeling Laboratory, NCAR, Boulder, CO 80307*
7) *Department of Chemistry, University of Toronto, ON, M5S 1A1, Canada*
8) *Department of Chemistry, University of Colorado, Boulder, CO 80309*

[†]Now at Department of Chemistry, University of Colorado, and NOAA Chemical Sciences Laboratory, Boulder, CO, USA
[‡]Now at California Air Resources Board, Sacramento, CA, USA
[#]Now at National Center for Atmospheric Research, Boulder, CO, USA
[§]Now at Pacific Northwest National Laboratory, Richland, WA, USA
[¶]Now at Department of Energy, Environmental, and Chemical Engineering, Washington University in St. Louis, MO, USA
[||]Now at German Environment Agency, Dessau-Roßlau, Germany

*Corresponding author: Caroline C. Womack.

Email: caroline.womack@noaa.gov

This PDF file includes:
Supplemental Text
Figures S1 to S13
Tables S1 to S4
SI References

Pages S1 to S28

Section S1. Additional F0AM model details

F0AM uses the Tropospheric Ultraviolet and Visible Radiation Model (TUV v5.2)[1] to determine wavelength-resolved solar flux that drives photochemistry. The UWFPS campaign did not include a direct measurement of the actinic flux, but total solar radiation was monitored hourly at the Utah Division of Air Quality (UDAQ) Hawthorn site[2]. To account for daily variability in the solar flux, the day with the highest solar radiation during the campaign, February 12, 2017, was assumed to represent a "clear-sky" day, and all other days were scaled relative to that day. We used that scaling factor to reduce the default photolysis frequencies in the TUV model from their clear sky values. We also constructed sensitivity tests to determine the sensitivity of the model to this assumption.

Because the O_3 depletion occurs in a lofted plume (Figure S10), we exclude dry deposition reactions, but include uptake of $ClNO_3$, $BrNO_3$, $BrNO_2$, HOCl, and HOBr on aerosol with a single uptake parameter for each compound taken from the literature[3-6], listed in Table S3. The F0AM model does not include any aerosol microphysics, so aerosol pH was not considered in the model. Uptake was treated as with first order kinetics, using the daily average aerosol surface area and single uptake parameters. The uptake parameter for N_2O_5 was determined directly for the Salt Lake area during the UWFPS campaign[7], and the average value of 0.076 was used here. This value is higher than many other modeling studies, so we conduct a sensitivity test in which we reduce this value by half to 0.04, and find little change to the model. N_2O_5 concentrations are low during the daytime plumes, and therefore its uptake has little impact on gas or particle abundance.

Section S2. CAM-chem/MUSICA model validation

The spatial (vertical and horizontal) and temporal variabilities of several key meteorological/chemical parameters in the CAM-chem/MUSICA model were evaluated against balloon-borne, airborne, and ground-based observations available for this study.

We use the sounding observations in Salt Lake City (40.77N, 111.95W), the closest sounding site to the studied area, to evaluate key meteorological parameters in the model that affect the dispersion and transport of pollutants in the model. Sounding balloons are released twice daily (00UTC and 12UTC), profiling temperature, humidity, and wind conditions from the surface to at least 20-30 km altitude. The sounding data was obtained from the University of Wyoming sounding archive: http://weather.uwyo.edu/upperair/sounding.html). Figure S14 (a) shows the vertical profiles of potential temperature, specific humidity, and winds between 27 January and 4 February, 2017, one PCAP period during UWFPS with the most severe air pollution. As shown, the stability condition in the lower-middle troposphere depicted by the potential temperature and specific humidity in the sounding profiles is reasonably well reproduced by the model, and the main transport pattern largely affected by the wind conditions in the sounding profiles is also reasonably well captured by the model. This implies the modeled meteorology is sufficiently reproducing boundary layer dynamics needed to study the impact of the industrial halogen emissions on the O_3 and particulate matter pollution in this region.

We then use in situ measurements of trace gases and fine particulate matter to evaluate the model's capability to capture the ozone and particulate matter pollution in this region. Airborne measurements of $O_{3,}$ reactive nitrogen, and chemical composition of PM_1 (particles smaller than ~1 micron in vacuum aerodynamic diameter measured by the Aerosol Mass Spectrometer, AMS) aboard the Twin Otter aircraft (see Methods in the main text) were used to evaluate the vertical distribution of key trace gases and speciated fine particulate matter (Figure S14 (b)). The model is capable of explicitly simulating the chemical evolution of aerosols in four size modes: Aitken mode, accumulation mode, coarse mode, as well as primary carbon mode. Liu *et al*Liu, Ma, Wang, Tilmes, Singh, Easter, Ghan and Rasch [8] and Zaveri *et al*Zaveri, Easter, Singh, Wang, Lu, Tilmes, Emmons, Vitt, Zhang, Liu, Ghan and Rasch [9] contain further details. In this work, the modeled PM_1 and $PM_{2.5}$ include Aitken, accumulation, primary carbon modes, as well as a fraction of coarse mode, and the fractional contributions of coarse mode to $PM_{2.5}$ and PM_1 are calculated based on size distributions described in Liu et al. (2016)[8]. Figure S14 (b) shows the mean vertical profiles of O_3 and PM_1 components measured during the take-off and landing stages near the Salt Lake City airport, during the aforementioned PCAP period (27 January – 4 February, 2017).

We note that the hourly FIVE-VCP-FOG emission inventory leads to a factor of 2 – 4 underestimation of NO_x and NH_3 compared to the observations in this region; as a result, ammonium nitrate, the major component of measured PM_1, is also underestimated by a factor of 3 – 4. A recent study measuring the tailpipe of heavy-duty trucks in Salt Lake City, found a strong dependency of NO_x emission factors with tailpipe temperature, and reduced efficiency of selective catalytic reduction (SCR) systems at colder temperatures [10]. This may partially explain an underestimate in mobile source NO_x emissions as the temperature-dependency of heavy-duty truck emissions are not currently taken into account in the FIVE mobile source emissions inventory. Furthermore, another recent study suggested that light-duty vehicular emissions of NH_3 in FIVE might also be significantly underestimated by ~40% when compared with satellite observations[11]. Since the goal of our modeling effort is to assess the role of primary halogen emissions on secondary chemistry, we scale up key organic and reactive nitrogen species to match aircraft observations, and reproduce regional chemical conditions observed during the field campaign: particulate organics were scaled up by a factor of 3, HONO and NO_x by 4, and NH_3 by 2. This improves agreement with speciated PM_1 and O_3 observations as shown in Figure S14 (b): modeled/measured ratios in the lowest 1 km are 0.42 ± 0.50, 0.37 ± 0.43, 1.01 ± 1.05, 1.04 ± 0.96, 0.66 ± 1.12, and 1.35 ± 0.36 for nitrate, ammonium, sulfate, particulate organics, particulate chloride, and O_3, respectively.

With the scaled up "top-down" reactive nitrogen emissions, the model predicts that ammonium nitrate is the dominant contributor to the total PM_1 mass. Interestingly, despite the sufficient supply of NO_x and NH_3 in the gas-phase, particulate ammonium nitrate is still underestimated by ~58% (Figure S14 (b)), implying that the oxidative capacity is likely still underestimated in the model even after scaling up primary precursor emissions to match observations. This is confirmed by another sensitivity test in which particulate organics, NO_x, and NH_3 emissions are scaled up as previously mentioned but HONO is kept unchanged; in this case the modeled NO_x and NH_3 are both overestimated yet ammonium nitrate is still underestimated by a factor of 4. Due to the lack of knowledge on the wintertime HONO emissions/chemistry in this region, we applied the same scaling factor of 4 for HONO and NO_x so the $HONO/NO_x$ ratio is consistent with the original emission inventories. We note that further investigation is needed on why NO_x, NH_3, and ammonium nitrate formation are being underestimated in emissions inventories and atmospheric chemistry models, but is beyond the scope of this study. Here, we constrain our model for key gas and aerosol-phase species in order to reasonably capture the general spatial/temporal variations of O_3 and PM pollution in the Salt Lake City region, and which is clearly a challenging phenomenon to model in the wintertime.

The model performance is further demonstrated by comparing with ground-based O_3 and $PM_{2.5}$ measurements from the EPA Air Quality System (AQS) network. Figure S15 (a) and (b) show modeled surface maximum daily 8-hour average (MDA8) O_3 and daily average $PM_{2.5}$ compared to the observations in all EPA AQS sites in the Northern Utah. As shown, the temporal variabilities in MDA8 O_3 and $PM_{2.5}$ are both well captured by the model, including all three pollution episodes (13-20 January, 27 January – 4 February, and 13-18 February) during the studied period. The modeled peak $PM_{2.5}$ during these episodes agree with the observations within 50% for most of the time in most of the sites. During these pollution episodes, the model predicts that ammonium nitrate is the major driver of the elevated $PM_{2.5}$, consistent with previous studies in this region[12] and the airborne observations shown in Figure S14 (b).

Section S3. Possible measurement interferences at high halogen concentrations.

When sampling large concentrations, such as in the nighttime plumes from US Magnesium, reagent ion reductions in the I- CIMS results in increased uncertainties (Table S1). When the reagent is no longer in excess, the observed species may be undercounted, and complex secondary ion chemistry within the instrument is possible, as described in the appendix of Veres *et al*Veres, Roberts, Burling, Warneke, de Gouw and Yokelson [13]. We therefore consider these highest measurements of halogens during the nighttime flights to be a lower bound. However, Figure S7 shows that there was no correlation between measured integrated flux and peak Cl_2 concentration, indicating that other sources of uncertainty are greater here than uncertainty introduced by possible reagent titration at the peak halogen concentration.

Additionally, known interferences in the I- CIMS include interconversion of some halogen species on the inlet, such as Cl_2 to HOCl and HOBr to Br_2[14]. Since both HOCl and HOBr are known photochemical products, we use the night flights to estimate an upper limit to their interconversion on the CIMS inlet and interior surfaces under the assumption that these species are not directly emitted. We find that there is a linear correlation between HOBr and Br_2, with a slope of roughly 3%, and a nonlinear correlation between HOCl and Cl_2 with a slope of 1% at Cl_2 concentrations below 100 ppb, but closer to 0.1% at higher levels (Figure S8). We do not expect these possible interferences to make any significant difference to the Br_2 and Cl_2 signals, but may represent a significant interference to the HOBr and HOCl signals. Our sensitivity tests (section II.c), however, show that these uncertainties do not change the results of the box model.

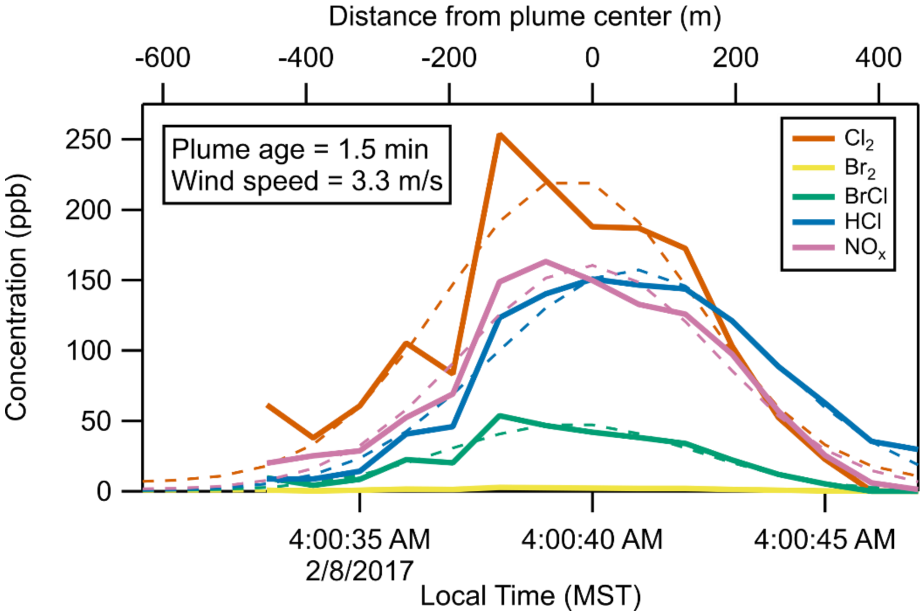

Fig. S1. A nighttime transect of the US Magnesium plume, measured on February 8, 2017 at approximately 4 am local time. The upper axis shows the approximate distance from the plume center, based on aircraft speed. The measured Br_2, Cl_2, BrCl, HCl and NO_x are shown in solid lines, while the dashed lines show the Gaussian fit to the data. The Gaussian fit was used to integrate across all the plumes, as some transects had missing data. The averaged wind speed across this transect was 3.3 m/s, and the plume transect was estimated to be 1.5 minute old at the time of measurement.

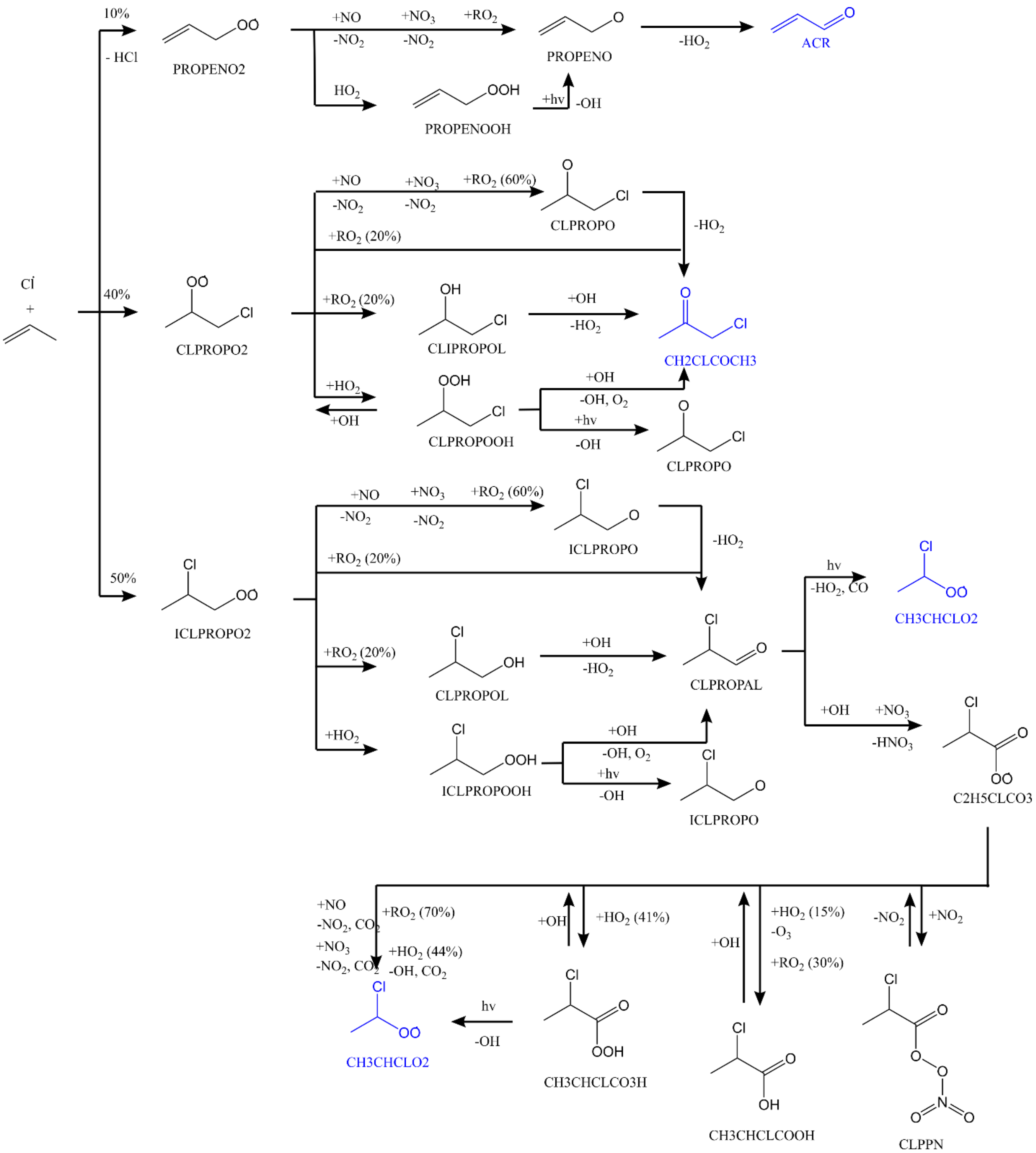

Fig. S2. The degradation scheme for Cl + C_3H_6 used in this analysis is shown. Following Xue et al[15], rate constants are taken from equivalent reactions of OH + C_3H_6. This mechanism is an expansion of the one shown in Fig 1 of Xue et al[15], with several more product channels explicitly described. The F0AM name is listed below each molecule. Blue lettering indicates that the species is in the MCM and that further degradation is already accounted for.

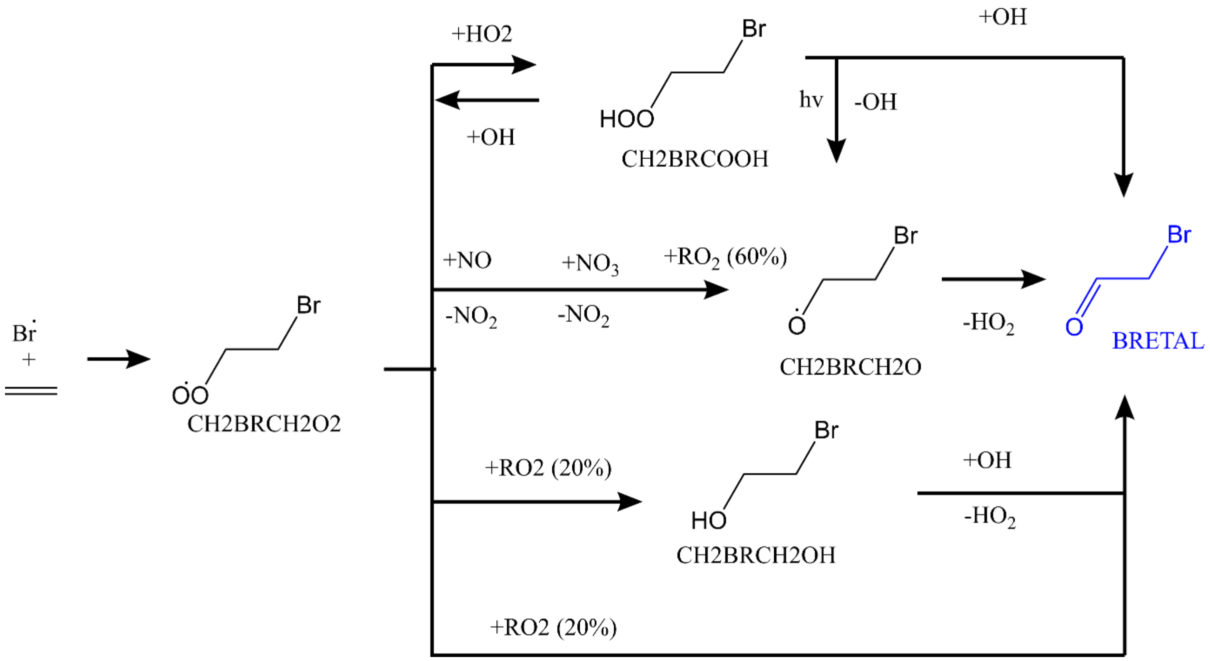

Fig. S3. The degradation scheme of Br + ethylene (C_2H_4). Mechanisms and reaction rates are taken directly from the analogous Cl + ethylene reaction that already exists in the MCM. Blue lettering indicates that the species and its further reactions are already in the MCM.

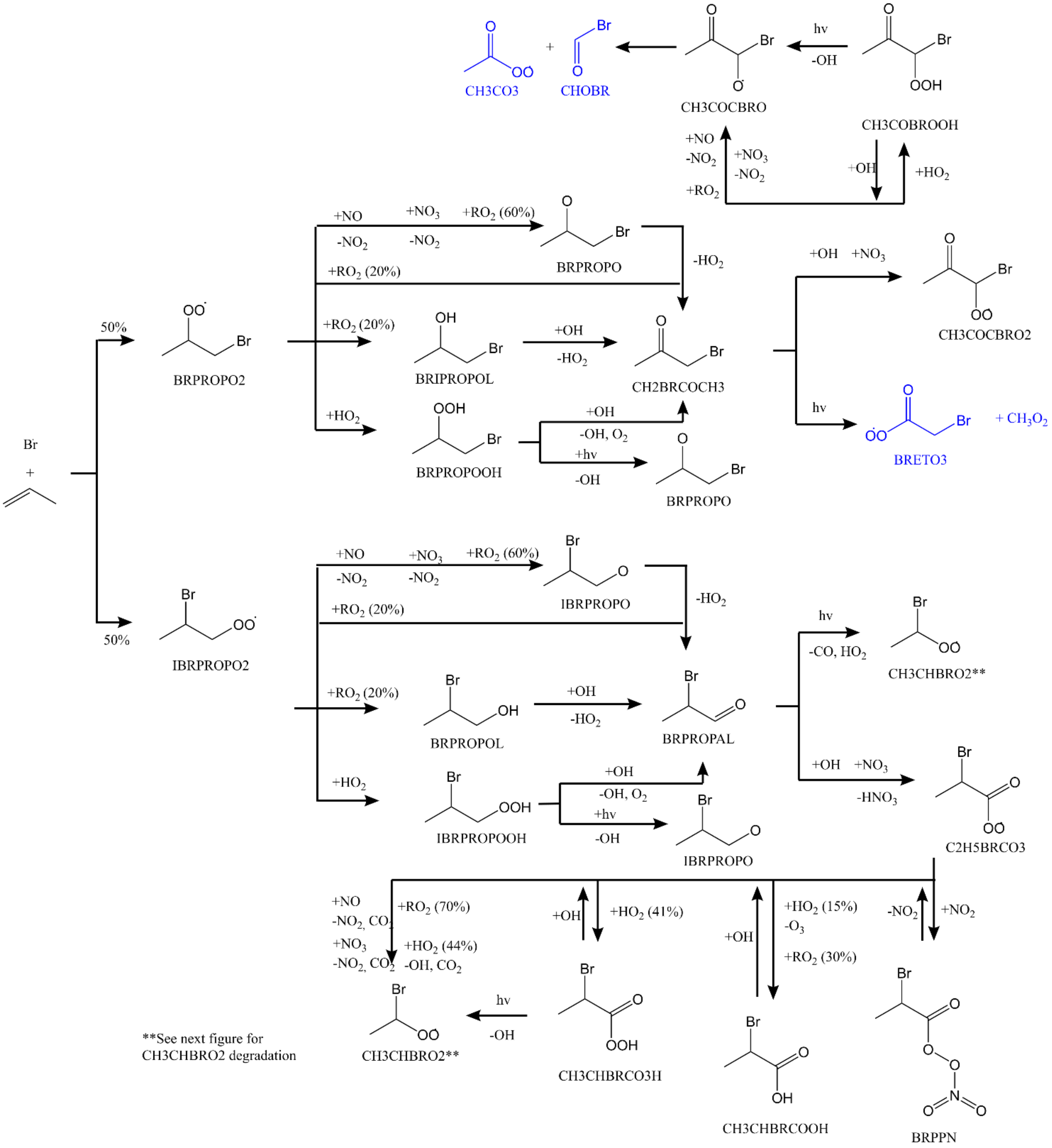

Fig. S4. The degradation scheme of Br + C_3H_6. Mechanisms and rates following the initial addition step (which is in Atkinson et al. 2008[16]), are analogous to Cl + C_3H_6, in Figure S2, but additional reactions were included to account for brominated analogues of the chlorinated species shown in blue in Figure S2. The complete degradation of CH_3CHBrO_2 is shown in Figure S5.

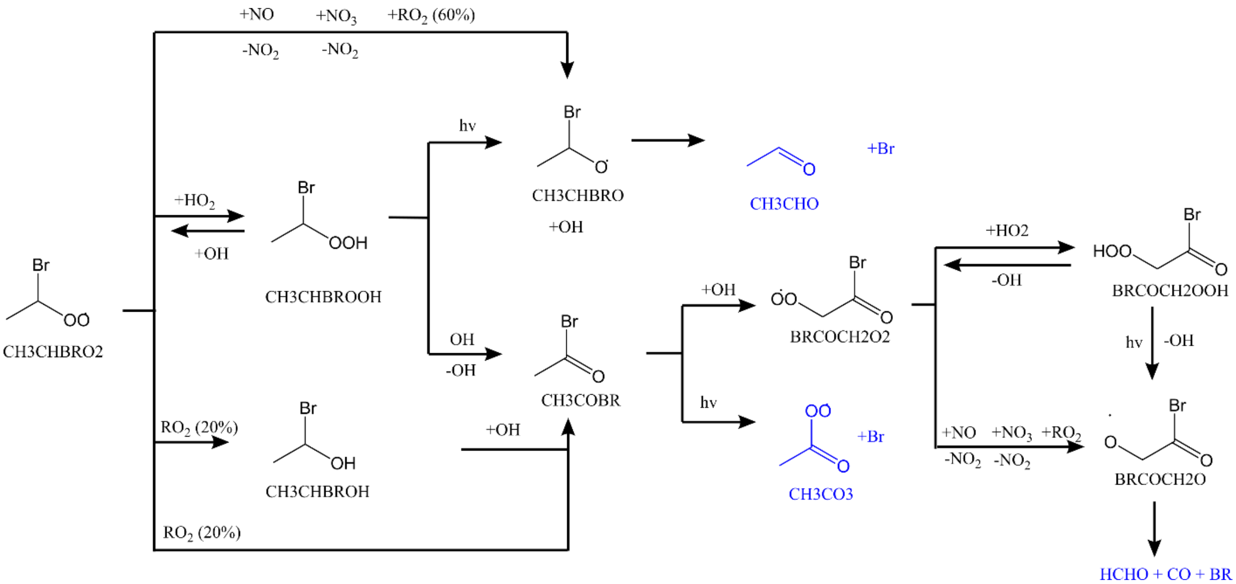

Fig. S5. The complete degradation of the species CH$_3$CHBrO$_2$, generated in the reaction of Br + C$_3$H$_6$ in Figure S14. Blue lettering indicate species that are already in the MCM.

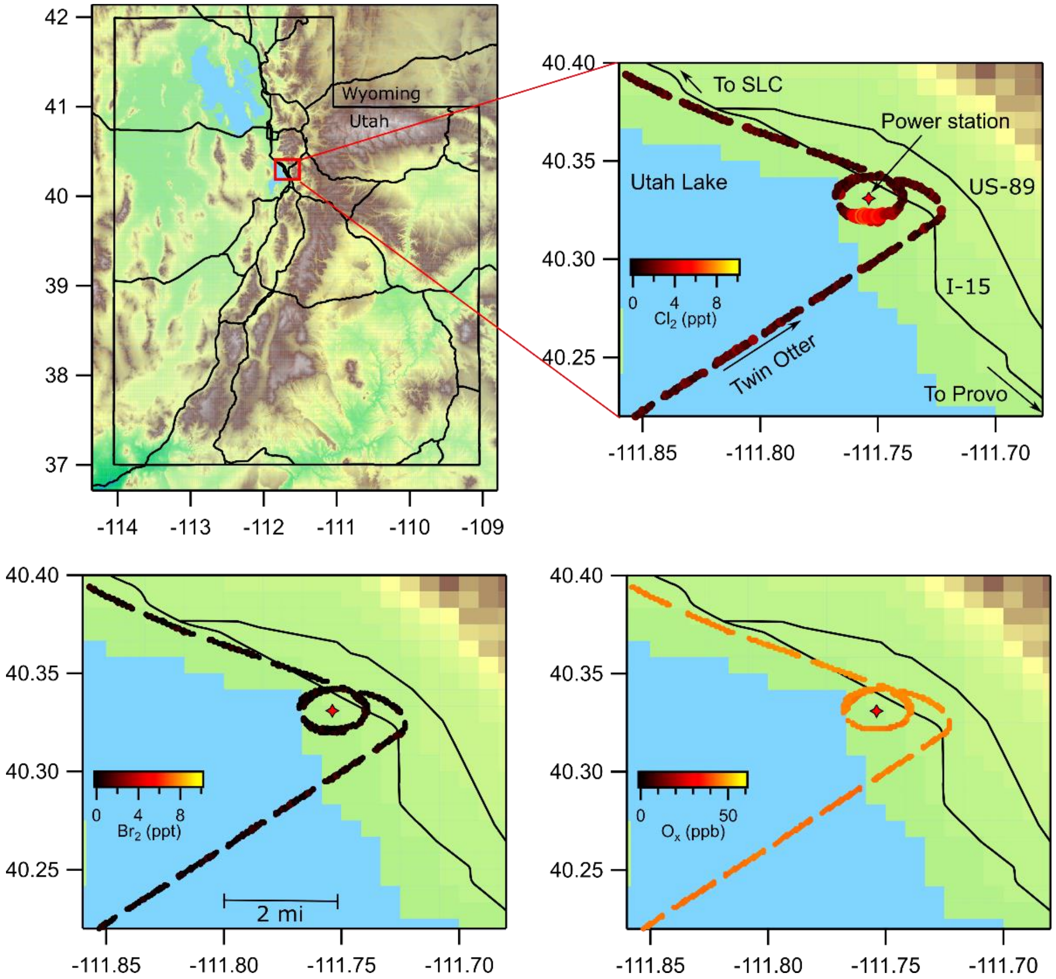

Fig. S6. The upper left panel shows a map of the state of Utah, with a red box highlighting a small portion of the Great Salt Lake area where the Twin Otter flew around a power station on the eastern shore of Utah Lake in the early morning hours of January 28, 2017. The upper right panel shows the zoomed in map colored by Cl_2 concentration, with the lower two panels showing the identical map colored by Br_2 and O_x. These traces demonstrate that while approximately 5 ppt of Cl_2 was observed in the emission plume of that power station, no Br_2 was observed, and no O_3 depletion was detected. Three other flights past this power station showed similar values but are not shown here.

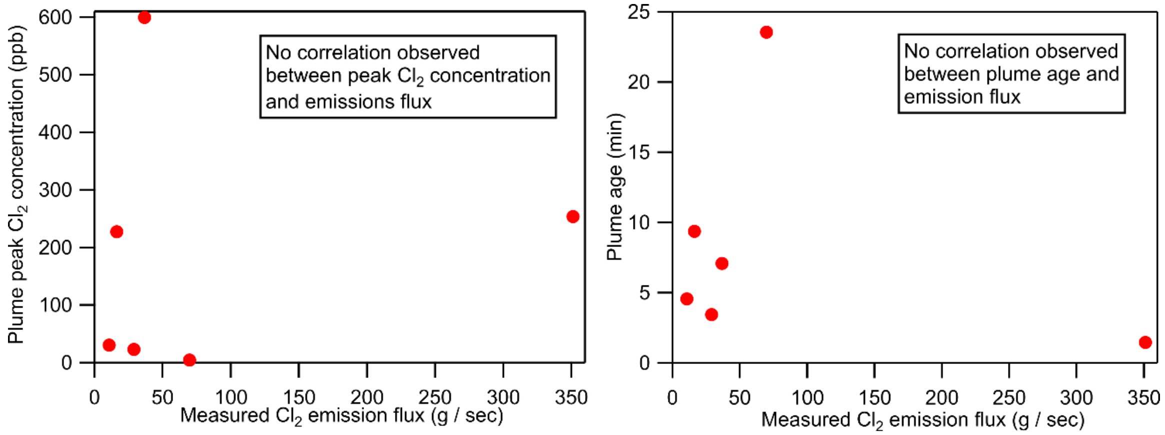

Fig. S7. No apparent correlation is observed between the observation-derived emission flux and the peak Cl_2 concentration or the plume age. This indicates that if I- CIMS reagent titration occurred in the largest peak (at 600 ppb Cl_2), it didn't lead to an anomalously low emission flux estimate. Furthermore, the lack of correlation between plume age and emissions flux is consistent with the assumption that dilution is the only loss process.

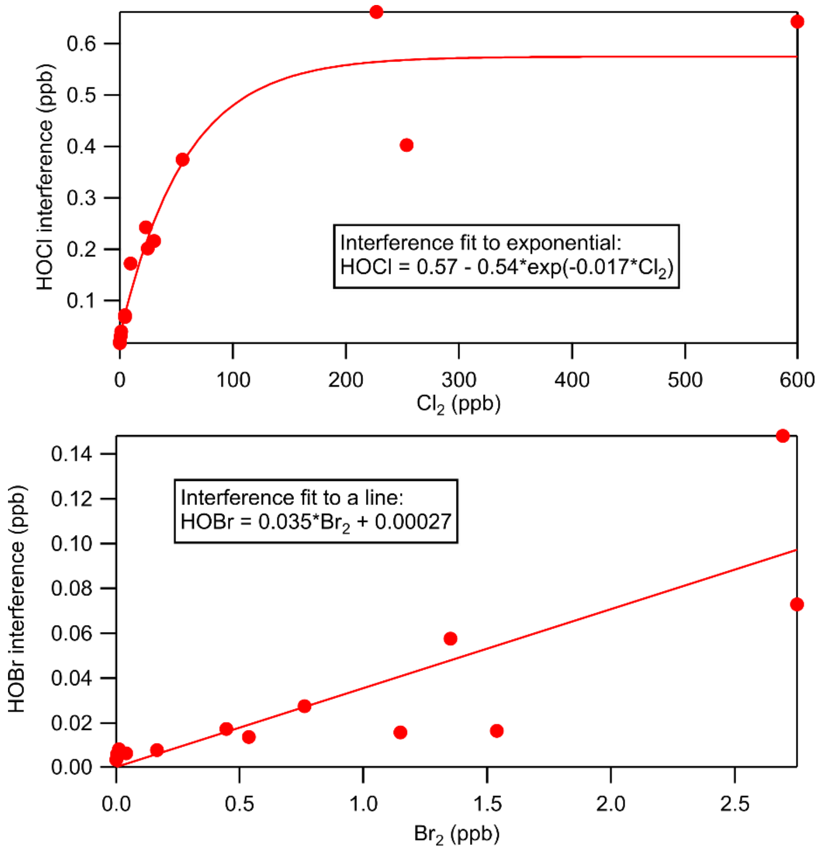

Fig. S8. Correlation plots between HOCl and Cl_2 (upper), and HOBr and Br_2 (lower). There are known interconversions of these two pair of species on instrument inlets, and so the nighttime flights were used to approximate these interconversions, assuming that HOBr and HOCl are photochemical products and are not directly emitted. Under this assumption, these plots indicate that the HOCl signal is roughly 1% of the Cl_2 at lower levels, and HOBr is roughly 3% of the Br_2. The direction of the potential interference is not clear, so Figure S12 shows the effect of both an increase and decrease in the HOBr by 3% and in HOCl by 1%.

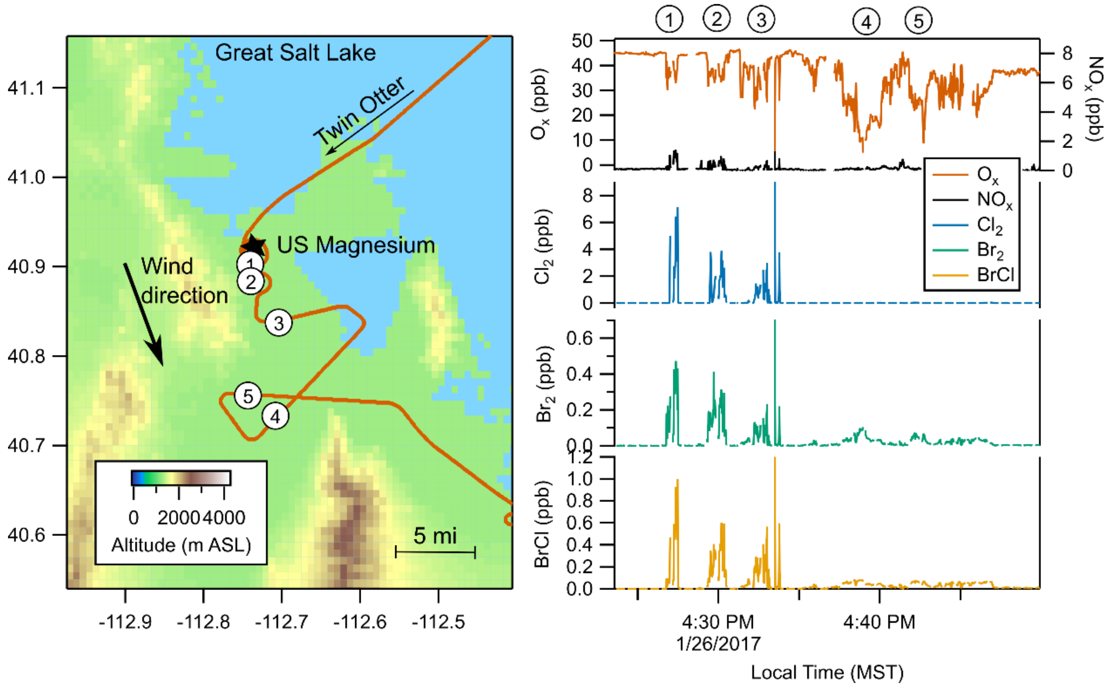

Fig. S9. A map and time series of the Twin Otter observations of high halogen concentrations and simultaneous O_3 depletions. Five plume transects are noted on both the map and the time series and show that close to the plant, halogens are high and O_3 depletion is well correlated with them. Transects 1 and 2 occurred at the same location but separated in altitude by 100 m, and did not pass directly through the center of the narrow plume, and therefore did not exhibit full O_3 depletion. Further downwind, the dihalogen species are largely gone, but the O_3 depletion remains until it recovers via entrainment from background air. Br_2 and BrCl are still present in transects 4 and 5 due to regeneration processes that Cl_2 does not undergo.

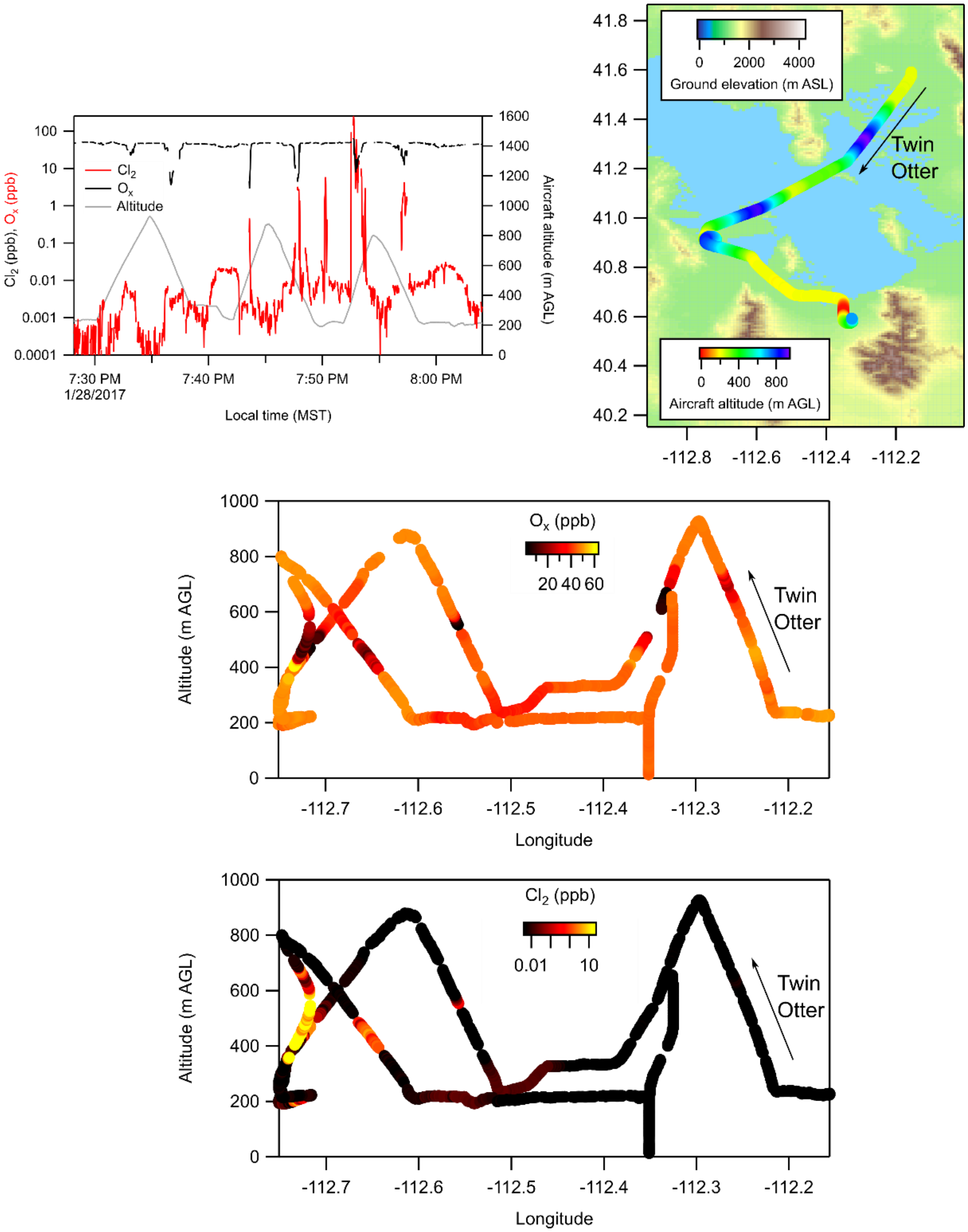

Fig. S10. Observations from the January 28 flights are shown, in which the aircraft profiled between 200 and 1000 m above ground level. The first panel shows a portion of the Twin Otter flight track, colored by the altitude of the aircraft, as it traveled west across the lake, circled the US Magnesium plant on the western side of the lake, and then returned east. The bottom two panels show curtain plots (altitude vs longitude) colored by Cl_2 and O_x concentrations during this portion of the flight. The presence of a lofted plume with high Cl_2 and depleted O_x concentrations isolated from the surface demonstrates the industrial, rather than natural source of the halogens. Natural halogen sources from the Great Salt Lake would be expected to show near-surface enhancement and a decreasing gradient with increasing altitude above the lake.

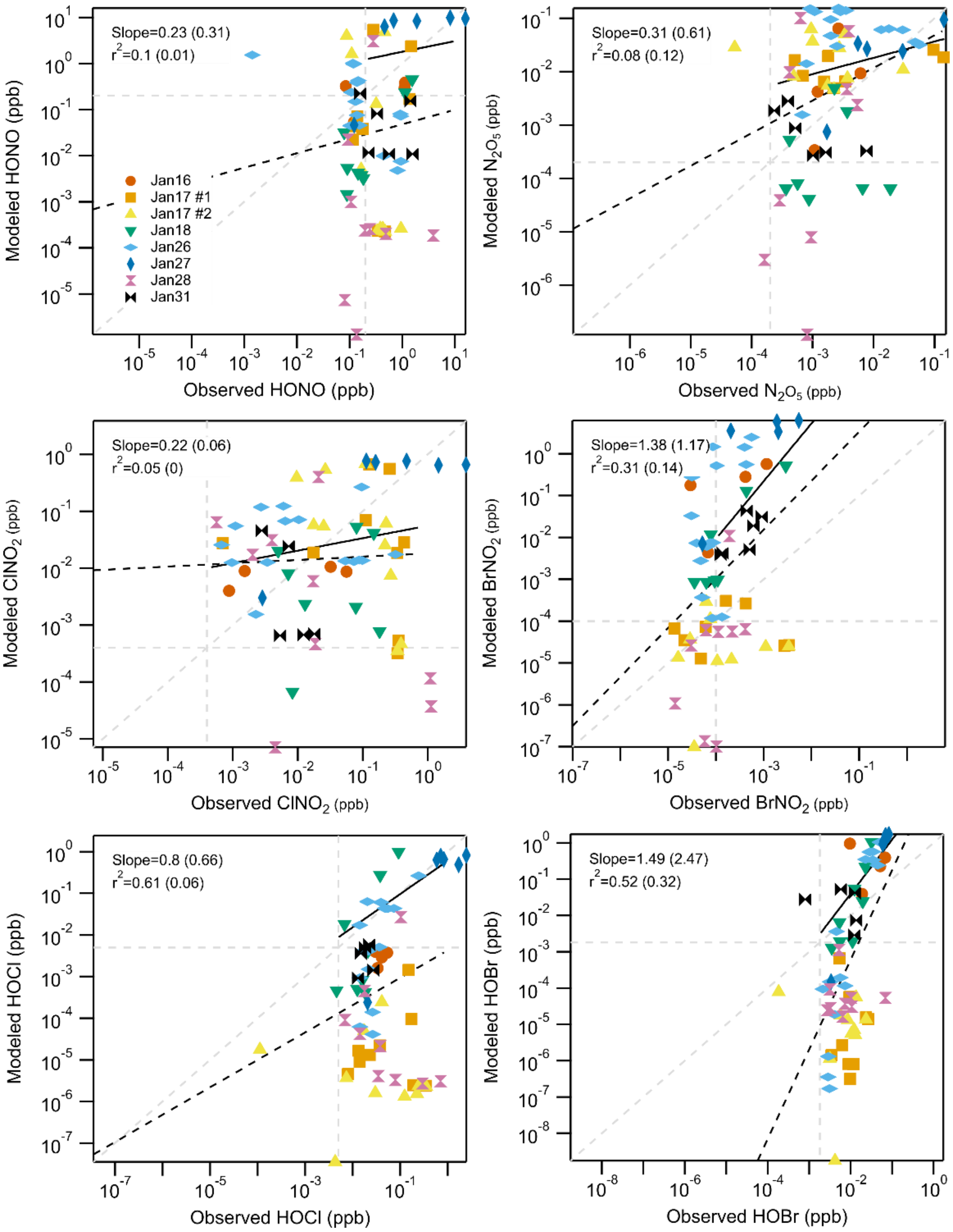

Fig. S11. Other observed species are compared to the model output. The light grey dashed lines show the limit of detection (LOD) for each species, as well as the 1:1 line. The data is fit in two ways, with solid line indicating a fit to all the data, and dashed line indicating a fit to only data points above the LOD. The data above the LOD for HONO, N_2O_5, $ClNO_2$, and HOCl fall approximately along the 1:1 line in black dashed line, but exhibit wider variability than the species shown in Figure 2. All these species are affected by the selection of the aerosol uptake parameter, the simplicity of the model, and HOBr and HOCl have a known inlet interference in the I- CIMS, as discussed in the text. However, as the sensitivity tests in Figure S13 demonstrate, the aerosol uptake does not significantly affect the conclusions of the model.

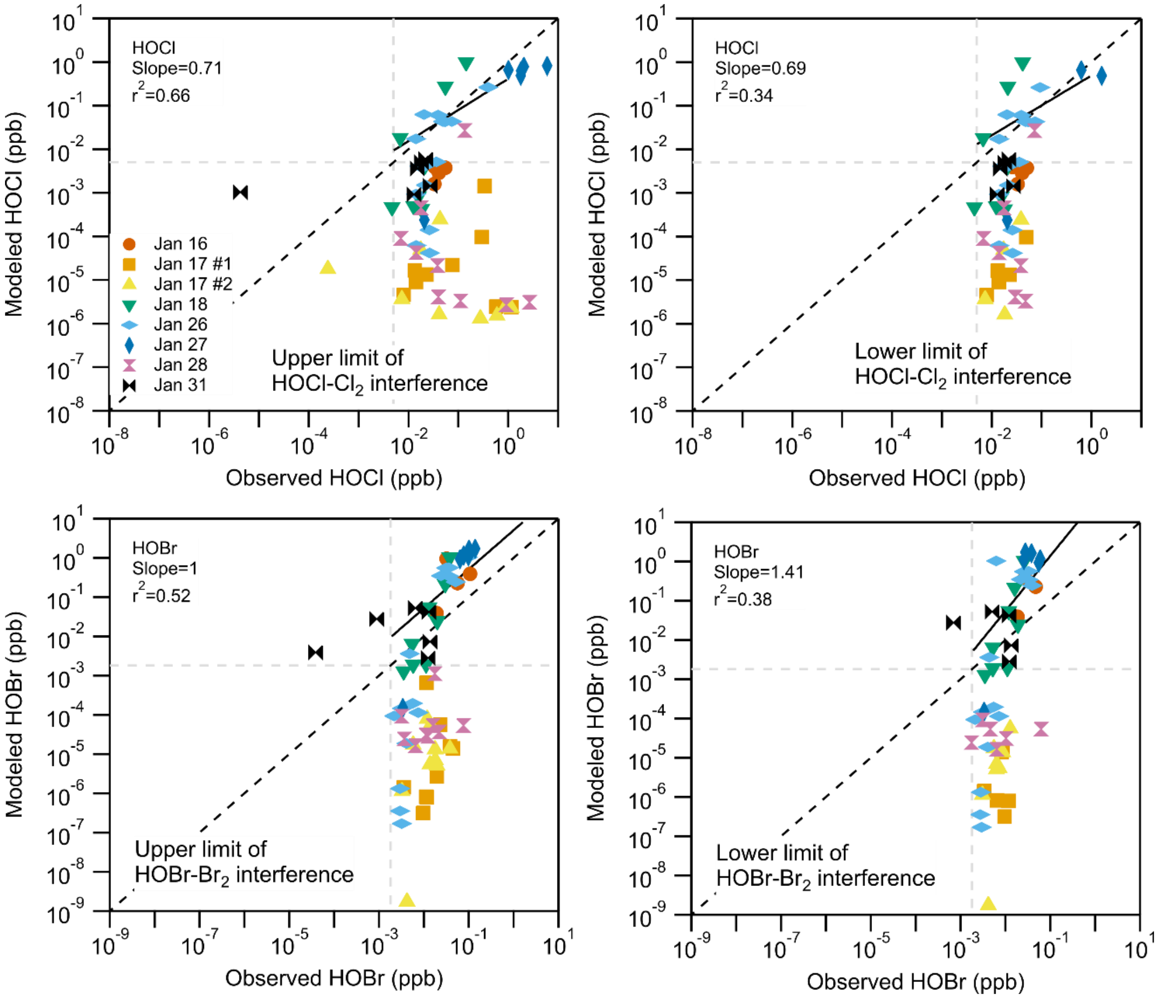

Fig. S12. Adjusted model-observation correlation plots, assuming that some of the HOBr and HOCl signal is from an inlet conversion of Br_2 or Cl_2. The observed HOBr and HOCl have been scaled up and down by 3% and 1% respectively. The resulting slopes do change somewhat, but do not bring the model into perfect alignment with the observations, indicating that there are other factors at play that also affect the model agreement for these species.

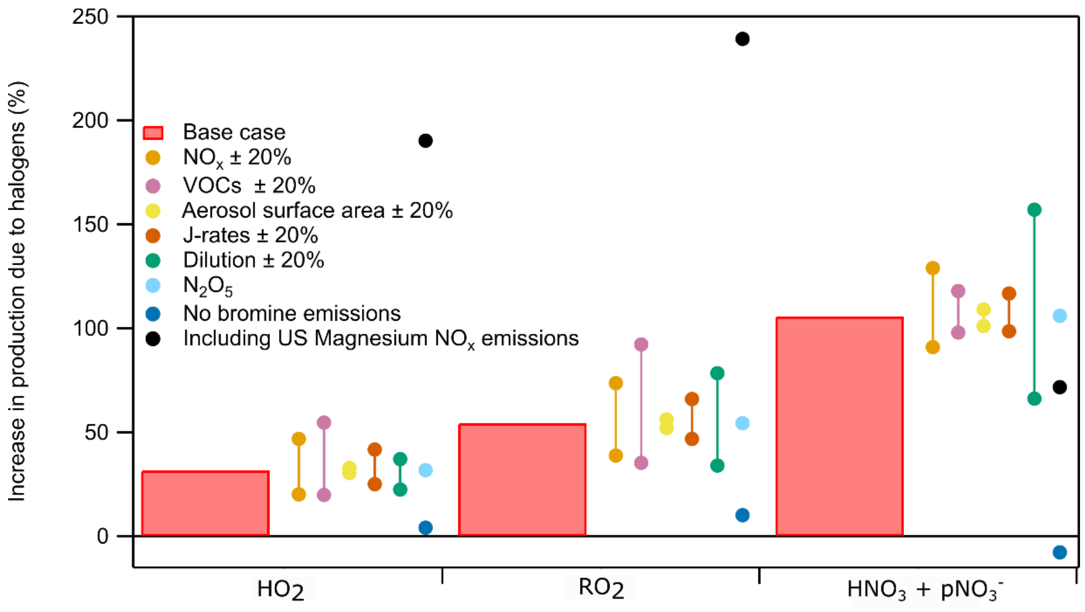

Fig. S13. The results of sensitivity simulations conducted to test various model assumptions. The red bars indicate the increase in production in HO_2, RO_2, and HNO_3 + pNO_3^- that can be attributed to halogens, derived from base case model simulation described in the main manuscript. The sets of colored markers to the right of each bar indicate the predicted increase in production when various model parameters are scaled up and down by 20%. NO_x (orange) and VOCs (purple), aerosol surface area (yellow), photolysis rates (red), and the dilution constant (green) all have an effect on the extent to which halogen enhance these species, but none fall below 0, indicating that all agree that halogens have a net enhancing effect. The light blue and black traces represent model runs with a lower N_2O_5 uptake coefficient (no change relative to the base case), and if all of US Magnesium's NO_x emissions were released from the same stack as the halogens (greatly magnifies the effect of the halogens). Finally, the dark blue trace indicates a model run in which only chlorine emissions were included, with no Br_2 or BrCl emissions. In this model run, HO_2 and RO_2 formation is not significantly enhanced by the chlorine emissions, and HNO_3 + pNO_3^- is actually slightly reduced by the chlorine emissions. This indicates that bromine plays a significant role in producing all three of these species in the base case.

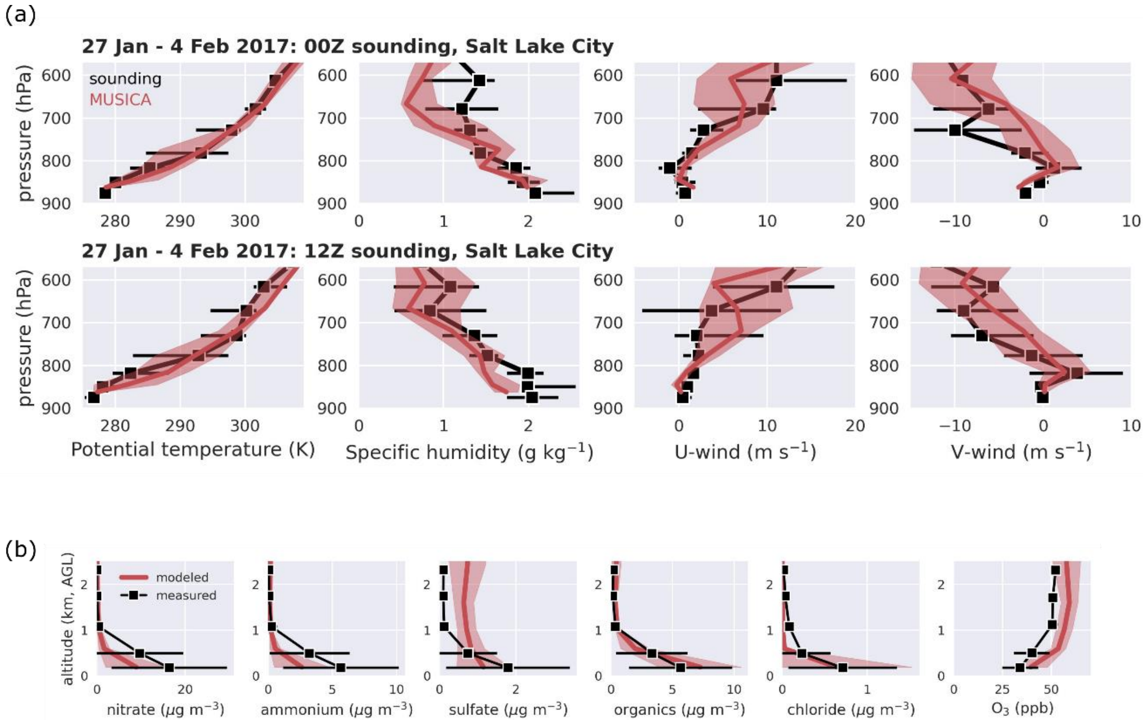

Fig. S14. (a) Comparison of average meterological soundings estimated by the CAM-chem model to those measured by twice-daily balloon soundings in Salt Lake City. (b) Comparison of average vertical profiles estimated the CAM-chem model to those measured by aircraft near Salt Lake City International Airport during UWFPS.

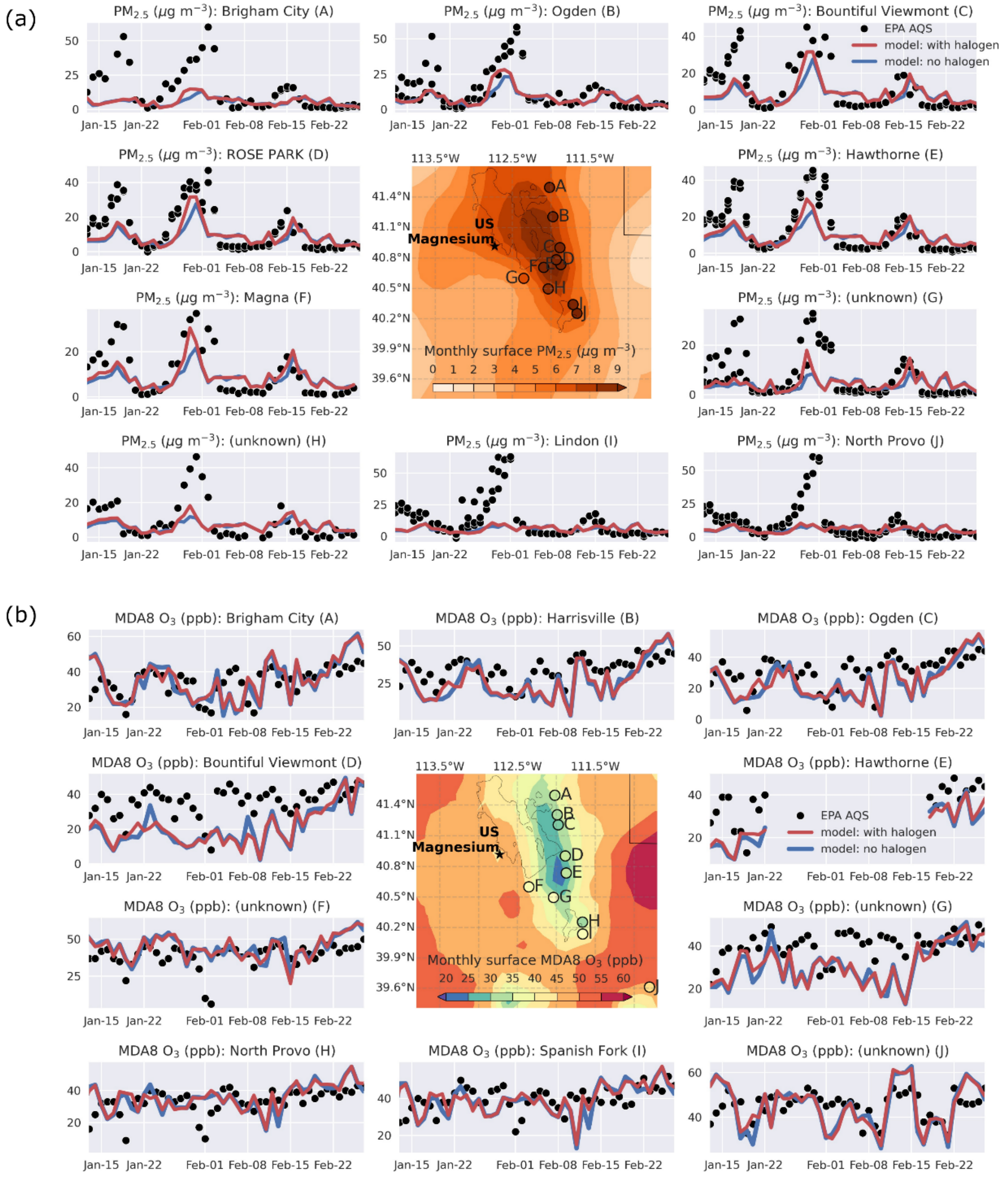

Fig. S15. The comparison of the CAM-chem model to daily PM$_{2.5}$ (panel a) and O$_3$ (panel b) at 10 EPA Air Quality System (AQS) sites, labeled A though I on the center maps. The model tends to under-predict the formation of aerosol during pollution episodes, including the period between 27 January and 4 February which represents the data in Figure 4b in the main text, but represents both the shape of the vertical profiles and the temporal trends in pollution well.

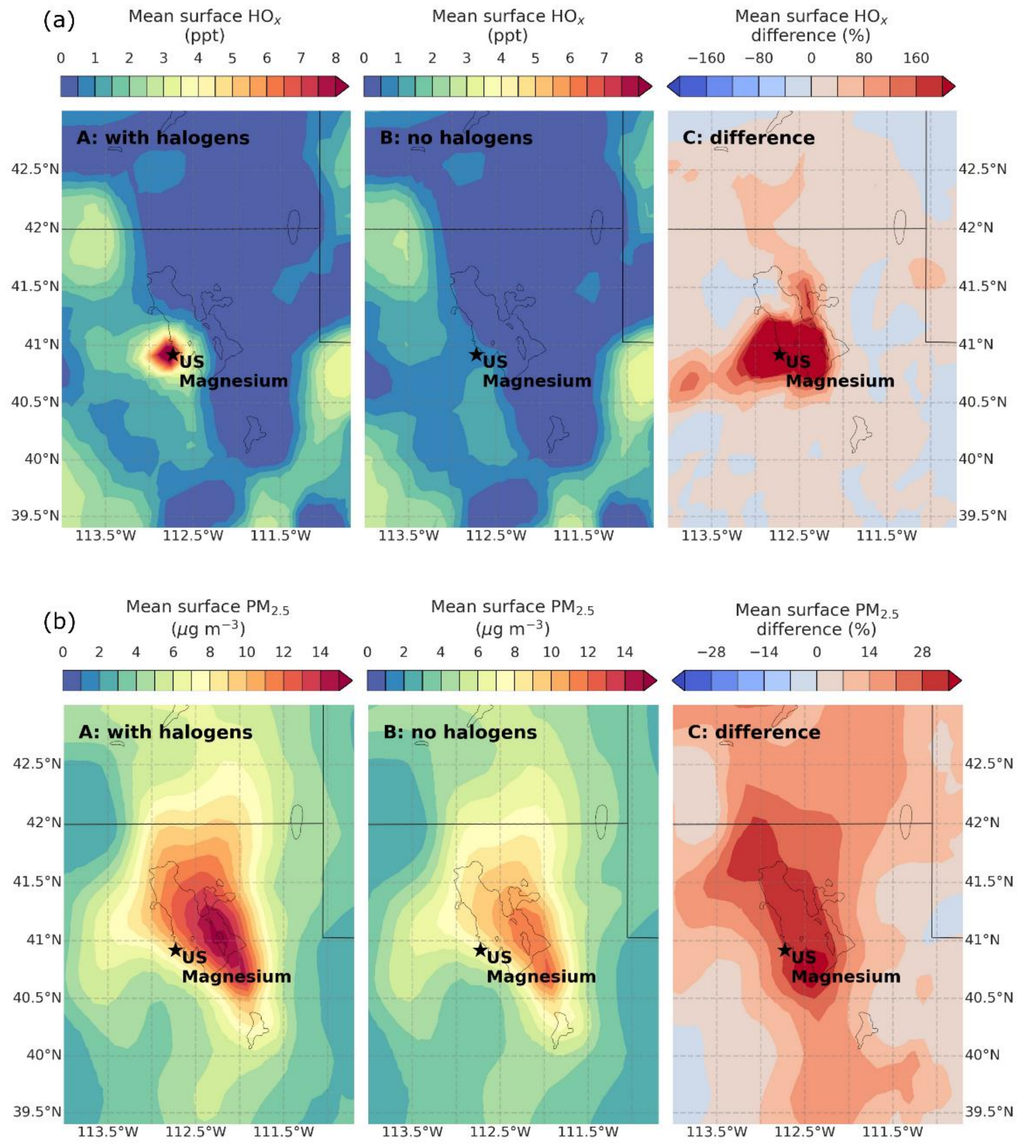

Fig. S16. Estimated HO_x and $PM_{2.5}$ during January 27 – February 4, 2017, with and without halogen emissions from US Magnesium. The rightmost panels show the percentage difference between the two model runs.

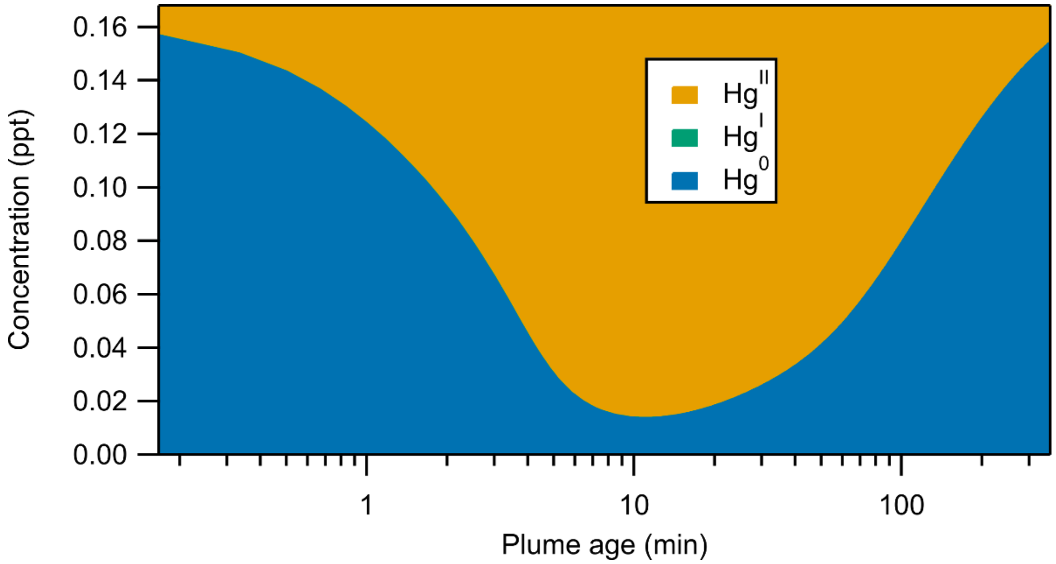

Fig. S17. A model run in which a small quantity of elemental mercury (Hg^0) was included as an initial condition and as a background species, and was converted to oxidized mercury (Hg^{II}) by reactions with Br radicals via Hg^I. A typical background value of 168 ppq was chosen based on average observations in the area. Dilution of the plume into the background air with this same quantity of Hg^0 is responsible for the slow disappearance of the Hg^{II} and the return of the Hg^0.

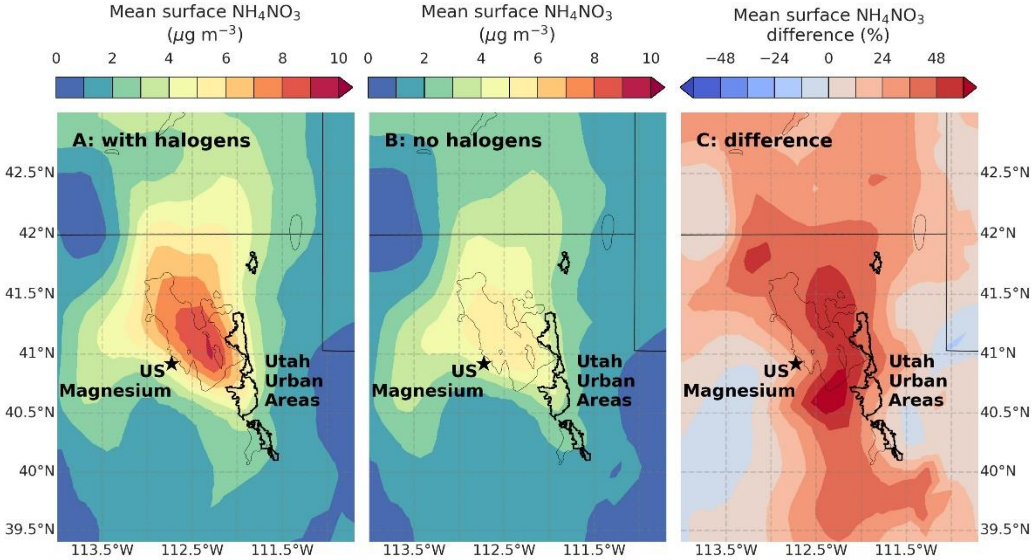

Fig. S18. The estimated ammonium nitrate during January 27 – February 4, 2017, with and without halogen emissions from US Magnesium. The rightmost panel shows the difference between the two model runs. This panel demonstrates that the majority of the change in $PM_{2.5}$ shown in figures 4 and S16 is due to an enhancement in ammonium nitrate formation.

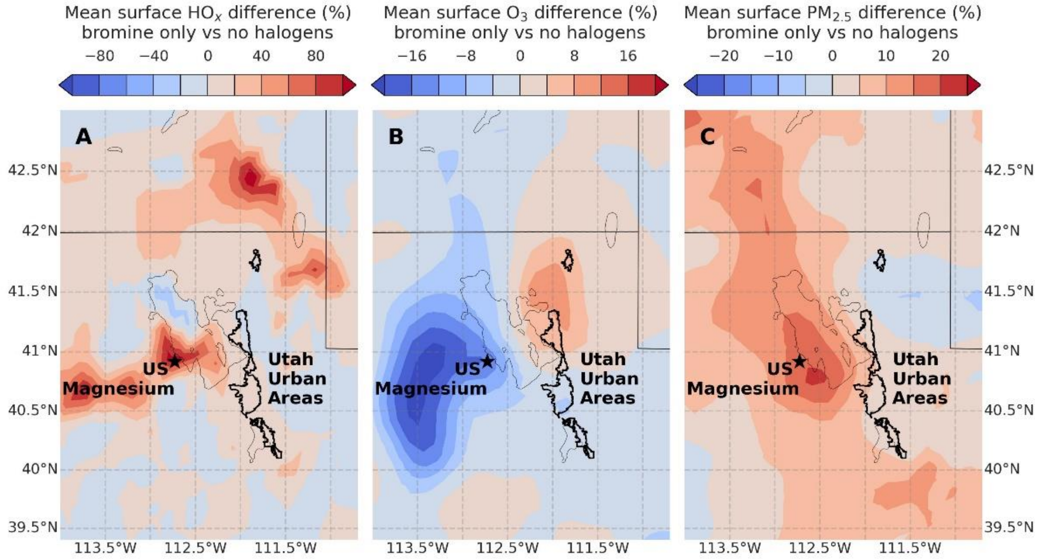

Fig. S19. The estimated change in mean surface HO_x, O_3, and $PM_{2.5}$ from the CAM-chem model when only bromine (no chlorine) emissions from US Magnesium are included. The effect on O_3 is not significantly different from that in figure 4 in the main text, but the effect on HO_x and $PM_{2.5}$ is less strong, indicating that bromine chemistry dominates the O_3 depletion, but chlorine chemistry is also playing a key role in HO_x, and therefore $PM_{2.5}$ production.

Table S1. Instruments on board the NOAA Twin Otter that provided the data used in this analysis, with the published lower detection limit and accuracy for each species. Note that additional inaccuracy may be introduced when sampling large concentrations of halogens, as indicated in Section S3 and Figures S7 and S8. Instruments were calibrated before, during, and after the UWFPS campaign using known standards.

Instrument	**Species**	**Lower detection limit**	**Accuracy**
I^-CIMS (Iodide chemical ionization mass spectrometry) **[17]**	Cl_2	0.4 ppt	30%
	Br_2	0.3 ppt	30%
	BrCl	0.2 ppt	50%
	HCl	160 ppt	30%
	$ClNO_2$	0.4 ppt	30%
	$BrNO_2$	0.1 ppt	50%
	HOCl	5.0 ppt	30%
	HOBr	1.8 ppt	50%
	HNO_3	60 ppt	30%
	HONO	200 ppt	50%
	N_2O_5	0.2 ppt	30%
NOxCaRD (Nitrogen oxide by cavity ringdown spectroscopy) **[18]**	NO_2	18 ppt	5%
	NO	14 ppt	5%
	O_3	28 ppt	5%
AMS (Aerosol mass spectrometer) **[19]**	pNO_3^-	0.06 ug / m3	30%
	pCl^-	0.15 ug / m3	30% but higher at higher pCl^- loadings
UHSAS (Ultrahigh sensitivity aerosol spectrometer) **[20]**	Aerosol surface area	-	34%

Table S2. The full mechanism used for halogen chemistry. The last column shows the reference, and is typically either IUPAC[16, 21] or JPL[6], or is cited separately.

Reaction	**Reaction Rate**	**Reference**
Chlorine inorganic reactions		
$Cl + O_3 \rightarrow ClO + O_2$	2.8e-11 x exp(-250/T)	IUPAC
$Cl + HO_2 \rightarrow OH + ClO$	4.4e-11 x (1.7 x exp(-620/T))	IUPAC
$Cl + HO_2 \rightarrow O_2 + HCl$	4.4e-11 x (1 - (1.7 x exp(-620/T)))	IUPAC
$Cl + H_2O_2 \rightarrow HO_2 + HCl$	1.1e-11 x exp(-980/T)	IUPAC
$ClOO + Cl \rightarrow ClO + ClO$	1.2e-11	JPL
$ClOO + Cl \rightarrow Cl_2 + O_2$	2.3e-10	JPL
$OClO + Cl \rightarrow ClO + ClO$	3.2e-11 x exp(170/T)	IUPAC
$Cl + Cl_2O_2 \rightarrow Cl_2 + ClOO$	7.6e-11 x exp(65/T)	IUPAC
$Cl + HOCl \rightarrow Cl_2 + OH$	3.4e-12 x exp(-130/T)	JPL
$Cl + NO_2 \rightarrow ClNO_2$	k_0 = 1.8e-31 x (T/300)^-2.0 k_∞ = 1.0e-10 x (T/300)^-1.0	JPL
$Cl + NO_3 \rightarrow ClO + NO_2$	2.4e-11	IUPAC
$Cl + ClNO \rightarrow Cl_2 + NO$	5.8e-11 x exp(100/T)	JPL
$Cl + ClNO_3 \rightarrow Cl_2 + NO_3$	6.2e-12 x exp(145/T)	IUPAC
$Cl + O_2 \rightarrow ClOO$	k_0 = 2.2e-33 x (T/300)^-3.1 k_∞ = 1.8e-10	JPL
$ClOO \rightarrow Cl + O_2$	k_{eq} = 6.6e-25 x exp(2502/T) k = $k_{Cl+O2 \rightarrow ClOO}$ / k_{eq}	JPL
$OH + Cl_2 \rightarrow HOCl + Cl$	3.6e-12 x exp(-1200/T)	IUPAC
$ClO + HO_2 \rightarrow O_2 + HOCl$	2.2e-12 x exp(340/T)	IUPAC
$OH + ClO \rightarrow HCl + O_2$	4.4e-13 x exp(300/T)	IUPAC

$OH + ClO \rightarrow HO_2 + Cl$	6.8e-12 x exp(300/T)	IUPAC
$ClO + O \rightarrow O_2 + Cl$	6.8e-12 x exp(300/T)	IUPAC
$ClO + ClO \rightarrow Cl_2 + O_2$	1.0e-12 x exp(-1590/T)	IUPAC
$ClO + ClO \rightarrow OClO + Cl$	3.5e-13 x exp(-1370/T)	IUPAC
$ClO + ClO \rightarrow Cl + ClOO$	3.0e-11 x exp(-2450/T)	IUPAC
$ClO + ClO \rightarrow Cl_2O_2$	k_0 = 1.6e-32 x (T/300)^-4.5 k_∞ = 3.0e-12 x (T/300)^-2	JPL
$Cl_2O_2 \rightarrow ClO + ClO$	k_{eq} = 1.72e-27 x exp(8649/T) k = $k_{ClO+ClO \rightarrow CL2O2}$ / k_{eq}	JPL
$ClO + NO \rightarrow Cl + NO_2$	6.2e-12 x exp(295/T)	IUPAC
$ClO + NO_2 \rightarrow ClNO_3$	k_0 = 1.8e-31 x (T/300)^-3.4 k_∞ = 1.5e-11 x (T/300)^-1.9	JPL
$OH + OClO \rightarrow HOCl + O_2$	1.4e-12 x exp(600/T)	IUPAC
$OClO + NO \rightarrow ClO + NO_2$	1.1e-13 x exp(350/T)	IUPAC
$OH + HCl \rightarrow H_2O + Cl$	1.7e-12 x exp(-230/T)	IUPAC
O + HCl → OH + Cl	1.0e-11 x exp(-3300/T)	JPL
$OH + Cl_2O_2 \rightarrow HOCl + ClOO$	6.0e-13 x exp(670/T)	JPL
$OH + HOCl \rightarrow H_2O + ClO$	5.0e-13	IUPAC
O + HOCl → OH + ClO	1.7e-13	JPL
$OH + ClNO_2 \rightarrow HOCl + NO_2$	2.4e-12 x exp(-1250/T)	IUPAC
$OH + ClNO_3 \rightarrow HOCl + NO_3$	1.2e-12 x exp(-330/T)	IUPAC
$O + ClNO_3 \rightarrow ClO + NO_3$	3.6e-12 x exp(-840/T)	JPL
Chlorine – organic reactions		
Cl + alkanes (C1 – C6)	Already in MCM	
$Cl + C_2H_4 \rightarrow CH_2CLCH_2O_2$	k_0 = 1.85e-29 x (T/300)^-3.3 k_∞ = 6.0e-10 fc = 0.4	IUPAC
$Cl + C_3H_6 \rightarrow$ HCl + PROPENO2	2.7e-10 Φ = 0.1	See Fig S2
$Cl + C_3H_6 \rightarrow$ CLPROPO2	k_0 = 4.0e-28 k_∞ = 2.8e-10 Φ = 0.4	See Fig S2
$Cl + C_3H_6 \rightarrow$ ICLPROPO2	k_0 = 4.0e-28 k_∞ = 2.80e-10 Φ = 0.5	See Fig S2
$Cl + C_2H_2 \rightarrow CHOCl + CO + HO_2$***	k_0 = 6.1e-30 x (T/300)^-3.0 k_∞ = 2.0e-10	IUPAC
$Cl + HCHO \rightarrow HCl + HO_2 + CO$	8.1e-11 x exp(-34/T)	IUPAC
$Cl + CH_3CHO \rightarrow CH_3CO_3 + HCl$	8.0e-11	IUPAC
$Cl + C_2H_5CHO \rightarrow C_2H_5CO_3 + HCl$	1.3e-10	IUPAC
$Cl + C_3H_7CHO \rightarrow C_3H_7CO_3 + HCl$	3.1e-11 x exp(410/T)	[15]
$Cl + C_3H_7CHO \rightarrow$ BUTALO2 + HCl	5.5e-12 x exp(410/T)	[15]
$Cl + CH_3COCH_3 \rightarrow HCl + CH_3COCH_2O_2$	3.2e-11 x exp(-815/T)	IUPAC
Cl + MEK → MEKAO2 + HCl	1.4e-11 x exp(80/T)	IUPAC
Cl + MEK → MEKBO2 + HCl	1.4e-11 x exp(80/T)	IUPAC
Cl + MEK → MEKCO2 + HCl	2.4e-12 x exp(80/T)	IUPAC
Cl + MACR → MACO3 + HCl	4.86e-11 x exp(380/T) x 0.45	[15]
Cl + DIEK → DIEKAO2 + HCl	2.4e-11	[15]
Cl + DIEK → DIEKBO2 + HCl	2.4e-11	[15]
Cl + HEX3ONE → HEX3ONAO2 + HCl	1.05e-10	[15]
Cl + HEX3ONE → HEX3ONBO2 + HCl	2.3e-11	[15]
Cl + HEX3ONE → HEX3ONCO2 + HCl	1.8e-11	[15]
Cl + HEX3ONE → HEX3ONDO2 + HCl	1.8e-11	[15]
$Cl + CH_3OH \rightarrow HCl + HCHO + HO_2$	5.5e-11	IUPAC

Cl + C_2H_5OH → HCl + CH_3CHO + HO_2	5.5e-11 x exp(155/T)	[15]
Cl + C_2H_5OH → HCl + $HOCH_2CH_2O_2$	4.8e-12 x exp(155/T)	[15]
Cl + HCOOH → HCl + CO_2 + H_2O	1.9e-13	IUPAC
Cl + CH_3CO_2H → HCl + CH_3O_2 + CO_2	2.64e-14	IUPAC
Cl + CH_3O_2 → ClO + HCHO + HO_2	1.6e-10 x 0.5	JPL
Cl + CH_3O_2 → HCl + CH_2OO	1.6e-10 x 0.5	JPL
Cl + $C_2H_5O_2$ → ClO + HO_2 + CH_3CHO	7.4e-11	JPL
Cl + $C_2H_5O_2$ → HCl + CH_3CHOO	7.7e-11	JPL
Cl + CH_3OOH → HCl + CH_3O_2	3.54e-11	[15]
Cl + CH_3OOH → HCHO + OH + HCl	2.36e-11	[15]
CH_3O_2 + ClO → ClOO + HO_2 + HCHO	3.3e-12 x exp(-115/T)	JPL
Cl + OXYL → OXYLO2 + HCl	1.5e-10	[22]
Cl + TOLUENE → C6H5CH2O2 + HCl	5.9e-11	[22]
Cl + TM124B → TM124BO2 + HCl	3.6e-10	[22]
Bromine – inorganic		
Br + O_3 → BrO + O_2	1.7e-11 x exp(-800/T)	IUPAC
Br + HO_2 → HBr + O_2	7.7e-12 x exp(-450/T)	IUPAC
Br + NO_2 → $BrNO_2$	k_0 = 4.2e-31 x (T/300)^-2.4 k_∞ = 2.7e-11	IUPAC
Br + NO_3 → BrO + NO_2	1.6e-11	IUPAC
$BrNO_3$ + Br → Br_2 + NO_3	4.9e-11	[23]
Br_2 + OH → HOBr + Br	2.0e-11 x exp(240/T)	IUPAC
BrO + OH → HO_2 + Br	1.8e-11 x exp(250/T)	IUPAC
BrO + O → Br + O_2	1.9e-11 x exp(230/T)	IUPAC
BrO + HO_2 → HOBr + O_2	4.5e-12 x exp(500/T)	IUPAC
BrO + BrO → Br + Br + O_2	2.4e-12 x exp(40/T)	JPL
BrO + BrO → Br_2 + O_2	1.5e-12 x exp(230/T) x 1.6 x exp(-190/T)	JPL
BrO + NO → NO_2 + Br	8.7e-12 x exp(260/T)	IUPAC
BrO + NO_2 → $BrNO_3$	k_0 = 4.7e-31 x (T/300)^-3.1 k_∞ = 1.8e-11 fc = 0.4	IUPAC
HBr + OH → H_2O + Br	6.7e-12 x exp(155/T)	IUPAC
HBr + O → OH + Br	5.8e-12 x exp(-1500/T)	JPL
HOBr + O → OH + BrO	1.2e-10 x exp(-430/T)	IUPAC
$BrNO_3$ + O → OH + BrO	1.9e-11 x exp(215/T)	IUPAC
Bromine – organics		
Br + HCHO → HO_2 + CO + HBr	7.7e-12 x exp(-580/T)	IUPAC
Br + CH_3CHO → CH_3CO_3 + HBr	1.8e-11 x exp(-460/T)	IUPAC
Br + CH_3COCH_3 → $CH_3COCH_2O_2$ + HBr	1.66e-10 x exp(-7000/T)	[24]
Br + C_2H_6 → $C_2H_5O_2$ + HBr	2.36e-10 x exp(-6411/T)	[25]
Br + C_3H_8 → i-$C_3H_7O_2$ + HBr	8.77e-11 x exp(-4330/T)	[25]
Br + C_3H_6 →BRPROPO2	3.6e-12 Φ = 0.5	See Fig S4
Br + C_3H_6 → IBRPROPO2	3.6e-12 Φ = 0.5	See Fig S4
Br + C_2H_4 → $CH_2BRCH_2O_2$	2.80e-13.*exp(224./T).*(M.*0.21.*7.5e-12)./((M.*0.21.*7.5e-12) + 8.5e12.*exp(-3200./T));	IUPAC
Br + C_2H_2 → CHOBr + CO + HO_2	6.35e-15 x exp(440/T)	IUPAC
Bromine – chlorine cross reactions		
BrO + ClO → BrCl + O_2	4.1e-13 x exp(290/T)	JPL
BrO + ClO → Br + ClOO	2.3e-12 x exp(260/T)	JPL

$\mathrm{BrO + ClO \rightarrow Br + OClO}$	9.5e-13 x exp(550/T)	JPL
$\mathrm{Br + OClO \rightarrow BrO + ClO}$	2.6e-11 x exp(-1300/T)	JPL
$\mathrm{Br + Cl_2O_2 \rightarrow BrCl + ClOO}$	5.9e-12 x exp(-170/T)	JPL

Table S3. Heterogeneous chemistry uptake coefficients used in the model

Reaction	Uptake coefficient	Reference
$\mathrm{ClNO_3 + Aer \rightarrow HOCl + HNO_3}$	0.024	[5]
$\mathrm{ClNO_3 + HBr + Aer \rightarrow BrCl + HNO_3}$	0.1	[3]
$\mathrm{ClNO_3 + HCl + Aer \rightarrow Cl_2 + HNO_3}$	0.1	[3]
$\mathrm{BrNO_3 + Aer \rightarrow HOBr + HNO_3}$	0.02	[5]
$\mathrm{BrNO_3 + HCl + Aer \rightarrow BrCl + HNO_3}$	0.9	JPL
$\mathrm{BrNO_2 + HCl + Aer \rightarrow BrCl + HONO}$	0.1	[26]
$\mathrm{HOCl + HBr + Aer \rightarrow BrCl + H_2O}$	0.04	JPL
$\mathrm{HOBr + HCl + Aer \rightarrow BrCl}$	0.1	[3]
$\mathrm{HOBr + HBr + Aer \rightarrow Br_2}$	0.1	JPL
$\mathrm{N_2O_5 + Aer \rightarrow 1.78{*}HNO_3 + 0.22{*}ClNO_2}$	0.076	[7]

Table S4. Photolysis rates used in the model. The JnXX value indicates the rate constant in F0AM.

Reaction	Photolysis rate
$\mathrm{ClNO_2 + hv \rightarrow Cl + NO_2}$	Jn23
$\mathrm{Br_2 + hv \rightarrow Br + Br}$	Jn24
$\mathrm{BrO + hv \rightarrow Br + O}$	Jn25
$\mathrm{HOBr + hv \rightarrow Br + OH}$	Jn26
$\mathrm{BrNO_2 + hv \rightarrow Br + NO_2}$	Jn27
$\mathrm{BrNO_3 + hv \rightarrow Br + NO_3}$	Jn28
$\mathrm{BrNO_3 + hv \rightarrow BrO + NO_2}$	Jn29
$\mathrm{BrCl + hv \rightarrow Br + Cl}$	Jn31
$\mathrm{Cl_2 + hv \rightarrow Cl + Cl}$	Jn32
$\mathrm{ClO + hv \rightarrow Cl + O}$	Jn33
$\mathrm{ClNO_3 + hv \rightarrow Cl + NO_3}$	Jn34
$\mathrm{ClNO_3 + hv \rightarrow ClO + NO_2}$	Jn35
$\mathrm{HOCl + hv \rightarrow Cl + OH}$	Jn36
$\mathrm{OClO + hv \rightarrow ClO + O}$	Jn37
$\mathrm{Cl_2O_2 + hv \rightarrow Cl + ClOO}$	Jn38
$\mathrm{ClOO + hv \rightarrow Cl + O2}$	Jn39

Table S5. A summary of the six model parameters optimized for each model, as well as jcorr, the corrective factor applied to all the photolysis reactions. The first five parameters indicate the starting conditions of each species. The final row shows the parameters used for the average model, in which Cl_2, dilution and jcorr are averaged, and Br_2, BrCl, and HCl are scaled relative to Cl_2 based on the emissions flux measurements in Table 1.

Date	**Cl_2 (ppb)**	**Br_2 (ppb)**	**BrCl (ppb)**	**HCl (ppb)**	**NO (ppb)**	**Dilution (s^{-1})**	**jcorr**
16Jan	1	4	0.05	20	2	0.00025	0.574
17Jan #1	85	1	10	20	40	0.00008	0.730
17Jan #2	85	1	10	20	40	0.00008	0.730
18Jan	100	5	20	5	2	0.0001	0.720
26Jan	105	15	25	20	10	0.00018	0.561
27Jan	200	20	10	5	30	0.00035	0.825
28Jan	100	2	10	10	40	0.00015	0.772
31Jan	20	8	1	10	10	0.00005	0.569
Average	*100*	*3*	*22*	*117*	--	*0.00015*	*0.68*

(1) Madronich, S.; McKenzie, R. L.; Björn, L. O.; Caldwell, M. M. Changes in biologically active ultraviolet radiation reaching the Earth's surface. *J. Photoch. Photobio. B.* **1998**, *46* (1), 5-19. DOI: http://doi.org/10.1016/S1011-1344(98)00182-1.

(2) Baasandorj, M.; Brown, S. S.; Hoch, S.; Crosman, E.; Long, R.; Silva, P.; L., M.; I., H.; Martin, R.; R., B.; et al. *2017 Utah Winter Fine Particulate Study Final Report*; 2018. https://www.esrl.noaa.gov/csd/groups/csd7/measurements/2017uwfps/finalreport.pdf (accessed 2022-11-28).

(3) Badia, A.; Reeves, C. E.; Baker, A. R.; Saiz-Lopez, A.; Volkamer, R.; Koenig, T. K.; Apel, E. C.; Hornbrook, R. S.; Carpenter, L. J.; Andrews, S. J.; et al. Importance of reactive halogens in the tropical marine atmosphere: a regional modelling study using WRF-Chem. *Atmos. Chem. Phys.* **2019**, *19* (5), 3161-3189. DOI: https://doi.org/10.5194/acp-19-3161-2019.

(4) Romer, P. S.; Wooldridge, P. J.; Crounse, J. D.; Kim, M. J.; Wennberg, P. O.; Dibb, J. E.; Scheuer, E.; Blake, D. R.; Meinardi, S.; Brosius, A. L.; et al. Constraints on Aerosol Nitrate Photolysis as a Potential Source of HONO and NO_x. *Environ. Sci. Technol.* **2018**, *52* (23), 13738-13746. DOI: https://doi.org/10.1021/acs.est.8b03861.

(5) Sherwen, T.; Schmidt, J. A.; Evans, M. J.; Carpenter, L. J.; Großmann, K.; Eastham, S. D.; Jacob, D. J.; Dix, B.; Koenig, T. K.; Sinreich, R.; et al. Global impacts of tropospheric halogens (Cl, Br, I) on oxidants and composition in GEOS-Chem. *Atmos. Chem. Phys.* **2016**, *16* (18), 12239-12271. DOI: https://doi.org/10.5194/acp-16-12239-2016.

(6) Chemical kinetics and photochemical data for use in atmospheric studies. Evaluation No. 17 http://jpldataeval.jpl.nasa.gov/ (accessed 2022-11-28).

(7) McDuffie, E. E.; Womack, C. C.; Fibiger, D. L.; Dube, W. P.; Franchin, A.; Middlebrook, A. M.; Goldberger, L.; Lee, B. H.; Thornton, J. A.; Moravek, A.; et al. On the contribution of nocturnal heterogeneous reactive nitrogen chemistry to particulate matter formation during wintertime pollution events in Northern Utah. *Atmos. Chem. Phys.* **2019**, *19* (14), 9287-9308. DOI: https://doi.org/10.5194/acp-19-9287-2019.

(8) Liu, X.; Ma, P. L.; Wang, H.; Tilmes, S.; Singh, B.; Easter, R. C.; Ghan, S. J.; Rasch, P. J. Description and evaluation of a new four-mode version of the Modal Aerosol Module (MAM4) within version 5.3 of the Community Atmosphere Model. *Geosci. Model Dev.* **2016**, *9* (2), 505-522. DOI: https://doi.org/10.5194/gmd-9-505-2016.

(9) Zaveri, R. A.; Easter, R. C.; Singh, B.; Wang, H.; Lu, Z.; Tilmes, S.; Emmons, L. K.; Vitt, F.; Zhang, R.; Liu, X.; et al. Development and Evaluation of Chemistry-Aerosol-Climate Model CAM5-Chem-MAM7-MOSAIC: Global Atmospheric Distribution and Radiative Effects of Nitrate Aerosol. *J. Adv. Model Earth Sy.* **2021**, *13* (4), e2020MS002346. DOI: https://doi.org/10.1029/2020MS002346.

(10) Bishop, G. A.; Haugen, M. J.; McDonald, B. C.; Boies, A. M. Utah Wintertime Measurements of Heavy-Duty Vehicle Nitrogen Oxide Emission Factors. *Environ. Sci. Technol.* **2022**, *56* (3), 1885-1893. DOI: https://doi.org/10.1021/acs.est.1c06428.

(11) Cao, H.; Henze, D. K.; Cady-Pereira, K.; McDonald, B. C.; Harkins, C.; Sun, K.; Bowman, K. W.; Fu, T.-M.; Nawaz, M. O. COVID-19 Lockdowns Afford the First Satellite-Based Confirmation That Vehicles Are an Under-recognized Source of Urban NH_3 Pollution in Los Angeles. *Environ. Sci. Technol. Lett.* **2022**, *9* (1), 3-9. DOI: https://doi.org/10.1021/acs.estlett.1c00730.

(12) Womack, C. C.; McDuffie, E. E.; Edwards, P. M.; Bares, R.; de Gouw, J. A.; Docherty, K. S.; Dubé, W. P.; Fibiger, D. L.; Franchin, A.; Gilman, J. B.; et al. An Odd Oxygen Framework for Wintertime Ammonium Nitrate Aerosol Pollution in Urban Areas: NO_x and VOC Control as Mitigation Strategies. *Geophys. Res. Lett.* **2019**, *46* (9), 4971-4979. DOI: https://doi.org/10.1029/2019gl082028.

(13) Veres, P.; Roberts, J. M.; Burling, I. R.; Warneke, C.; de Gouw, J.; Yokelson, R. J. Measurements of gas-phase inorganic and organic acids from biomass fires by negative-ion proton-transfer chemical-ionization mass spectrometry. *J. Geophys. Res.* **2010**, *115* (D23), D23302. DOI: https://doi.org/10.1029/2010JD014033.

(14) Neuman, J. A.; Nowak, J. B.; Huey, L. G.; Burkholder, J. B.; Dibb, J. E.; Holloway, J. S.; Liao, J.; Peischl, J.; Roberts, J. M.; Ryerson, T. B.; et al. Bromine measurements in ozone depleted air over the Arctic Ocean. *Atmos. Chem. Phys.* **2010**, *10* (14), 6503-6514. DOI: https://doi.org/10.5194/acp-10-6503-2010. Lawler, M. J.; Sander, R.; Carpenter, L. J.; Lee, J. D.; von Glasow, R.; Sommariva, R.; Saltzman, E. S. HOCl and Cl_2 observations in marine air. *Atmos. Chem. Phys.* **2011**, *11* (15), 7617-7628. DOI: https://doi.org/10.5194/acp-11-7617-2011.

(15) Xue, L. K.; Saunders, S. M.; Wang, T.; Gao, R.; Wang, X. F.; Zhang, Q. Z.; Wang, W. X. Development of a chlorine chemistry module for the Master Chemical Mechanism. *Geosci. Model Dev.* **2015**, *8* (10), 3151-3162. DOI: https://doi.org/10.5194/gmd-8-3151-2015.

(16) Atkinson, R.; Baulch, D. L.; Cox, R. A.; Crowley, J. N.; Hampson, R. F.; Hynes, R. G.; Jenkin, M. E.; Rossi, M. J.; Troe, J.; Wallington, T. J. Evaluated kinetic and photochemical data for atmospheric chemistry: Volume IV – gas phase reactions of organic halogen species. *Atmos. Chem. Phys.* **2008**, *8* (15), 4141-4496. DOI: https://doi.org/10.5194/acp-8-4141-2008.

(17) Lee, B. H.; Lopez-Hilfiker, F. D.; Mohr, C.; Kurtén, T.; Worsnop, D. R.; Thornton, J. A. An iodide-adduct high-resolution time-of-flight chemical-ionization mass spectrometer: Application to atmospheric inorganic and organic compounds. *Environ. Sci. Technol.* **2014**, *48* (11), 6309-6317. DOI: http://doi.org/10.1021/es500362a.

(18) Wild, R. J.; Edwards, P. M.; Dubé, W. P.; Baumann, K.; Edgerton, E. S.; Quinn, P. K.; Roberts, J. M.; Rollins, A. W.; Veres, P. R.; Warneke, C.; et al. A measurement of total reactive nitrogen, NO_y, together with NO_2, NO, and O_3 via cavity ring-down spectroscopy. *Environ. Sci. Technol.* **2014**, *48* (16), 9609-9615. DOI: http://doi.org/10.1021/es501896w.

(19) Bahreini, R.; Dunlea, E. J.; Matthew, B. M.; Simons, C.; Docherty, K. S.; DeCarlo, P. F.; Jimenez, J. L.; Brock, C. A.; Middlebrook, A. M. Design and operation of a pressure-controlled inlet for airborne sampling with an aerodynamic aerosol lens. *Aerosol Sci. Tech.* **2008**, *42* (6), 465-471. DOI: https://doi.org/10.1080/02786820802178514.

(20) Liao, J.; Brock, C. A.; Murphy, D. M.; Sueper, D. T.; Welti, A.; Middlebrook, A. M. Single-particle measurements of bouncing particles and in situ collection efficiency from an airborne aerosol mass spectrometer (AMS) with light-scattering detection. *Atmos. Meas. Tech.* **2017**, *10* (10), 3801-3820. DOI: http://doi.org/10.5194/amt-10-3801-2017.

(21) Atkinson, R.; Baulch, D. L.; Cox, R. A.; Crowley, J. N.; Hampson, R. F.; Hynes, R. G.; Jenkin, M. E.; Rossi, M. J.; Troe, J. Evaluated kinetic and photochemical data for atmospheric chemistry: Volume III - gas phase reactions of inorganic halogens. *Atmos. Chem. Phys.* **2007**, *7* (4), 981-1191. DOI: https://doi.org/10.5194/acp-7-981-2007.

(22) Shi, J.; Bernhard, M. J. Kinetic studies of Cl-atom reactions with selected aromatic compounds using the photochemical reactor-FTIR spectroscopy technique. *Int. J. Chem. Kinet.* **1997**, *29* (5), 349-358. DOI: https://doi.org/10.1002/(SICI)1097-4601(1997)29:5<349::AID-KIN5>3.0.CO;2-U.

(23) Orlando, J. J.; Tyndall, G. S. Rate Coefficients for the Thermal Decomposition of $BrONO_2$ and the Heat of Formation of $BrONO_2$. *J. Phys. Chem.* **1996**, *100* (50), 19398-19405. DOI: https://doi.org/10.1021/jp9620274.

(24) King, K. D.; Golden, D. M.; Benson, S. W. Kinetics of the gas-phase thermal bromination of acetone. Heat of formation and stabilization energy of the acetonyl radical. *J. Am. Chem. Soc.* **1970**, *92* (19), 5541-5546. DOI: https://doi.org/10.1021/ja00722a001.

(25) Seakins, P. W.; Pilling, M. J.; Niiranen, J. T.; Gutman, D.; Krasnoperov, L. N. Kinetics and thermochemistry of R + hydrogen bromide ↔ RH + bromine atom reactions: determinations of the heat of formation of ethyl, isopropyl, sec-butyl and tert-butyl radicals. *J. Phys. Chem.* **1992**, *96* (24), 9847-9855. DOI: https://doi.org/10.1021/j100203a050.

(26) Li, Q.; Fu, X.; Peng, X.; Wang, W.; Badia, A.; Fernandez, R. P.; Cuevas, C. A.; Mu, Y.; Chen, J.; Jimenez, J. L.; et al. Halogens Enhance Haze Pollution in China. *Environ. Sci. Technol.* **2021**, *55* (20), 13625-13637. DOI: https://doi.org/10.1021/acs.est.1c01949.